JOURNAL OF AIRCRAFT
Vol. 45, No. 5, September–October 2008

Generation of Aerodynamic Databases Using High-Order Singular Value Decomposition

L. S. Lorente,* J. M. Vega,† and A. Velazquez‡
Universidad Politecnica de Madrid, 28040 Madrid, Spain

DOI: 10.2514/1.35258

The fast generation of aerodynamic databases is important in the aeronautic industry because of its implication on both the cost and time needed to complete design cycles. This paper presents a method of generating those databases that uses a limited number of computational fluid dynamics computations, thereby saving CPU time. The method is based on a high-order singular value decomposition approach and is able to deal efficiently with complex airfoil flowfields that contain, simultaneously, two shock waves and a large separation region. This feature is critical because methods based on the singular value decomposition approach tend to encounter difficulties when dealing with shock wavelike structures. To illustrate the methodology, the flow around a two-dimensional airfoil is considered at a Reynolds number of 20×10^6 with three free parameters, namely, the Mach number, angle of attack, and flap deflection angle in the ranges of 0.4–0.8, $-3- + 3$ deg, and $-5- + 5$ deg, respectively. The method is robust in the sense that it is able to deal with very different flow topologies. Also, it is expected that it will contribute to significant savings in CPU time in aerodynamic database generation activities.

Nomenclature

C_D	=	drag coefficient
C_{FM}	=	flap momentum coefficient
C_{FD}	=	friction component of drag coefficient
C_L	=	lift coefficient
C_M	=	momentum coefficient
C_{PD}	=	pressure component of drag coefficient
C_p	=	pressure coefficient, $2P/(\rho_\infty U_\infty^2)$
$\bar{C}_p$	=	pressure coefficient divided by a reference value
d	=	shock wave thickness
L	=	distance between shock waves
M	=	Mach number
P	=	pressure
P_{xm}	=	threshold value of the pressure steepness of shock waves structures
U_∞	=	velocity at the outer freestream flow
$\bar{Z}$	=	airfoil thickness divided by a reference value
α	=	angle of attack
ΔP	=	pressure jump across the shock wave
δ	=	angle of the flap deflection
ρ_∞	=	density in the outer freesteam flow

Introduction

NOWADAYS, the use of computational fluid dynamics (CFD) is widespread in the aeronautic industry. The reason is that wind-tunnel campaigns are both expensive and limited to certain windows of time owing to the availability of the experimental facility. Nevertheless, numerical algorithms lack flexibility and, as every seasoned designer feels, the confidence gained after a wind-tunnel test cannot be matched by that provided by a simulation run. Improvement toward solving these two difficulties is becoming crucial in the practical application of CFD. Also, aeronautic companies are now listed on the stock exchange, which means that the time span from conceptual design to market is a critical factor. Design loops are performed within prescribed constraints of time and cost, and the engineer has to make the best out of these constraints and their own design tools. Therefore, the tendency is to emphasize the use of CFD and to keep wind-tunnel testing for the purposes of validation, cross checking, and analysis of the most complex cases.

One of the many aspects to be dealt with in the context of aerodynamics design is database generation. Usually, these databases are multiparametric, and thousands of computer runs are needed to fill them up. For instance, for a given 2-D airfoil, the engineer might be interested in determining the behavior of its aerodynamic coefficients and local surface pressure distribution as functions of the Reynolds and Mach numbers, the angle of attack, and the flap deflection angle. If he computes 5–10 values for each parameter, the whole database requires 5^4–10^4 simulation runs. This is not to mention the case in which geometry design parameters, such as those defining the shape functions used for airfoil shape generation, are accounted for or the case in which a full 3-D wing is considered. In this context, the cost advantage associated with the use of CFD may be offset by the sheer number of numerical simulations needed. The way out of this dilemma is, of course, to compute a limited, well-selected number of cases and to interpolate between them. However, the problem with interpolation is that accuracy degrades when either more than a few parameters (defining the database dimension) are involved or the distance between the available points in the parametric space is not small enough. An alternative method to plain interpolation, proposed by Bui-Thanh [1], consists of the combined use of interpolation and techniques based on either singular value decomposition (SVD) or proper orthogonal decomposition (POD): interpolation is carried out using SVD or POD modes that already contain global information of the whole parametric space instead of doing it locally, in the vicinity of the sought parameters. However, one of the difficulties associated with the use of the SVD/POD formulations in their original form is that they are not well suited to deal with flow topologies that present shock wavelike structures. In this context, the main objective of this paper is to present a method focused on the generation of aerodynamic databases containing airfoil flowfields that exhibit pressure and/or a suction side shock waves and large separated flow regions. The method is based on high-order singular value

Received 11 January 2008; revision received 18 April 2008; accepted for publication 18 April 2008.

*Ph.D. Student, Aerospace Propulsion and Fluid Mechanics Department, School of Aeronautics, Plaza del Cardenal Cisneros 3; luissantiago.lorente@upm.es.

†Professor, Applied Mathematics Department, School of Aeronautics, Plaza del Cardenal Cisneros 3; josemanuel.vega@upm.es.

‡Associate Professor, Aerospace Propulsion and Fluid Mechanics Department, School of Aeronautics, Plaza del Cardenal Cisneros 3; angel.velazquez@upm.es.

decomposition (HOSVD), which is a recent generalization of SVD to the case of parametric spaces having more than two dimensions.

POD-based methods have been used in aerodynamic applications for various purposes. For instance, Bui-Thanh et al. [2] dealt with data reconstruction, combining incomplete experimental and computational data to reconstruct full aerodynamic flowfields. An interesting feature of [2] is that the authors developed a strategy to minimize the sensitivity of the reconstructed results on the experimental error. A comparison between system identification techniques and POD in the context of unsteady aerodynamics has been done by Tang et al. [3]. The application of POD to particle image velocimetry with the aim of extracting information on the problem of vortex buffeting of an aircraft tail has been reported by Kim et al. [4]. Also, POD can be used to generate reduced-order aerodynamic models, which in turn allow the cost-efficient generation of aerodynamic databases out of a certain limited number of computational results. This has been done in a variety of contexts; see [5–8] for various examples, including the analysis of turbomachinery cascades [7]. POD and balanced realization methods have been proposed by Willcox and Peraire [9] to develop robust reduced-order models. And last, but not least, the use of POD and Volterra theory, such as it appears in [10–12] for aeroelastic applications, should be mentioned because of its implications in aerodynamics modeling. The interested reader can find a comprehensive review on the basic aspects of reduced-order modeling in Lucia et al. [13].

Regarding the organization of the present paper, the HOSVD technique is summarized first. Then, in the following section, a method is proposed to deal with shock wavelike structures in the flowfield. A test problem is stated next, and results are summarized and discussed. Finally, conclusions and concluding remarks are presented in the final section.

High-Order Singular Value Decomposition

HOSVD is an extension to tensors of SVD [14], which only applies to matrices. The SVD of a $m \times n$ matrix A leads to a decomposition $A = U \cdot D \cdot V^T$, where the superscript T stands for the transpose; U and V are appropriate orthogonal matrices, namely, such that $U \cdot U^T = I$ and $V \cdot V^T = I$; and D is a positive definite diagonal matrix with r nonzero elements, where r is precisely the rank of A (defined as usual) and the nonzero elements of D are called *singular values* of A. This decomposition can also be written in terms of the elements of A as

$$A_{ij} = \sum_{l=1}^{r} \delta_l u_{il} v_{jl}$$

where δ_l are the singular values and for varying l, and u_{il} and v_{jl} are the columns of U and V, respectively. These are both orthonormal systems and can be calculated as the eigenvectors associated with the nonzero eigenvalues of the (symmetric) matrices $A \cdot A^T$ and $A^T \cdot A$, respectively; the nonzero eigenvalues of these two matrices coincide and are the squares of the singular values of A. If such decomposition is truncated to $s < r$ terms, then the error in terms of the Frobenius norm

$$\|A\| = \sum_{i,j} (A_{ij})^2$$

is bounded by

$$[\sum_{l=s+1}^{r} (\delta_l)^2]^{1/2}$$

When this is small, an approximation of A exists that only requires the saving of $s \times (m + n)$ numbers (in fact, less than that if orthonormality relations are used) instead of the original $m \times n$ numbers required to save the matrix A, which is quite effective to compress A when s is small compared with both m and n. And this can, in fact, happen due to the inherent redundancy of A (namely, to patterns along the elements of A), which can be due to a physical law when A is a physical quantity.

The extension of all these to deal with a third-order $m \times n \times p$ tensor would be

$$A_{ijk} = \sum_{l=1}^{r} \delta_l u_{il} v_{jl} w_{kl} \tag{1}$$

where u_{il}, v_{jl}, and w_{kl} are the components of some orthonormal systems. The minimum value of r such that this decomposition is possible is called the *rank of the tensor A*. Unfortunately, both the determination of the rank of a tensor and the construction of effective algorithms to calculate minimal decompositions of tensors are open problems nowadays [15], except for some particular cases (e.g., $2 \times n \times n$ tensors). Furthermore, intended iterative algorithms converging to minimal decompositions should be constructed with care due to some subtleties [16], which are not encountered in matrices. Thus, some other, less restrictive decompositions have been pursued for tensors. One of these is

$$A_{ijk} = \sum_{i_1=1}^{r_1} \sum_{j_1=1}^{r_2} \sum_{k_1=1}^{r_3} \sigma_{i_1 j_1 k_1} u_{i i_1} v_{j j_1} w_{k k_1} \tag{2}$$

where $\sigma_{i_1 j_1 k_1}$ is a new third-order tensor and the vector systems $u_{i i_1}$, $v_{j j_1}$, and $w_{k k_1}$ are still orthornormal. This is precisely the HOSVD, which (as the SVD) is unique and can be calculated quite effectively as follows. The HOSVD modes are calculated as the (orthonormal) eigenvectors of the symmetric matrices B^1, B^2, and B^3, defined as

$$B^1_{il} = \sum_{j,k} A_{ijk} A_{ljk}$$

$$B^2_{jl} = \sum_{i,k} A_{ijk} A_{ilk}$$

and

$$B^3_{kl} = \sum_{i,j} A_{ijk} A_{ijl}$$

associated with nonzero eigenvalues, namely,

$$\sum_{j,k,l} A_{ijk} A_{ljk} u_{l i_1} = \alpha_{i_1} u_{i i_1} \tag{3a}$$

$$\sum_{i,k,l} A_{ijk} A_{ilk} v_{l j_1} = \beta_{j_1} v_{j j_1} \tag{3b}$$

$$\sum_{i,j,l} A_{ijk} A_{ijl} w_{l k_1} = \gamma_{k_1} w_{k k_1} \tag{3c}$$

Thus, r_1, r_2, and r_3 are the ranks of the matrices B^1, B^2, and B^3 and are called the ranks associated with the three indices of the tensor. Note that in matrices the ranks associated with both indices (i.e., rows and columns) both coincide and equal the rank of the matrix. In tensors, however, it could only be assured that r_1, r_2, and $r_3 \leq r$. Again, if the tensor exhibits inherent redundancy, then the sums in Eq. (2) can be truncated to $s_1 \leq r_1$, $s_2 \leq r_2$, and $s_3 \leq r_3$ terms, which produces a new decomposition that only requires the storage of $s_1 \times s_2 \times s_3 + s_1 \times m + s_2 \times n + s_3 \times p$ numbers instead of the original $m \times n \times p$ numbers that define the tensor A. Compression is large when s_1, s_2, and/or s_3 are small compared with m, n, and/or p, respectively. Such truncation involves an error, again, in terms of the Frobenius norm of the tensor,

$$\|A\| = \sum_{i,j,k} (A_{ijk})^2$$

that is bounded as

$$|\text{error}| \leq \sqrt{\sum_{i_1=s_1+1}^{r_1} \alpha_{i_1} + \sum_{j_1=s_2+1}^{r_2} \beta_{j_1} + \sum_{k_1=s_3+1}^{r_3} \gamma_{k_1}} \tag{4}$$

which gives an a priori estimate of the error in terms of the eigenvalues of Eqs. (3a–3c) even before calculating the reduced tensor (sometimes called the core tensor) $\sigma_{i_1 j_1 k_1}$. The latter tensor can be calculated from

$$\sigma_{i_1 j_1 k_1} = \sum_{i=1}^{m} \sum_{j=1}^{n} \sum_{k=1}^{p} A_{ijk} u_{ii_1} v_{jj_1} w_{kk_1} \tag{5}$$

which is obtained by multiplying Eq. (2) by u_{ii_1}, v_{jj_1}, and w_{kk_1}, adding in i, j, and k, and noting that these three systems of vectors are orthonormal.

Summarizing, given a third-order tensor A, it could be possible to write it as in Eq. (2), with the HOSVD modes calculated as the (unit) eigenvectors of Eqs. (3a–3c) associated with nonzero eigenvalues. Then, Eq. (2) is truncated invoking Eq. (4) and the reduced truncated tensor components are calculated by using Eq. (5). Fourth-, fifth-, and higher-order tensors are treated similarly.

Now, in usual aeronautic applications, a tensor A can result from, for example, snapshots giving the pressure field P along the surface of either a 2-D airfoil or a 3-D wing defined in terms of the spatial coordinate(s) and various parameters. In the test problem here, the tensor A will be defined from the pressure on either the pressure or the suction side of a 2-D airfoil whose points are labeled in terms of the horizontal spatial coordinate, x_i, for various values of three parameters: the Mach number M_j, the angle of attack α_k, and the flap deflection angle δ_l. Namely, a fourth-order tensor is defined as

$$P_{ijkl} = P(M_i, \alpha_j, \delta_k, x_l) \tag{6}$$

The HOSVD modes associated with the last index are a basis of a linear manifold in the space of possible pressure fields that is intended to effectively approximate the pressure field on the airfoil surface at any point of the parameter space. The problem is that, if the pressure field exhibits shock waves (or any other localized structure) whose position can move for varying values of the parameters, the number of required HOSVD modes (and thus the number of snapshots required to determine them) can be quite large. This is just because the final representation of the pressure field is made in terms of linear combinations of HOSVD modes, and linear combinations of pressure fields exhibiting shock waves at different positions can only accurately reconstruct a shock wave if the number of modes is somewhat large compared with the ratio L/d (which is usually quite large), where L is the distance between shock wave positions and d is the shock wave thickness. If this does not hold, the reconstructed shock wave splits the exact jump into combinations of multiple jumps, as in Fig. 1, in which a unique pressure jump is approximated by four jumps that result when using standard HOSVD without any a priori treatment of the shock wave (cf. Figure 10 for the same case treated with the method presented in this paper, which dramatically improves the approximation). Also, for the sake of comparison, results obtained by using direct linear and spline-based interpolations (no HOSVD) within the parametric space are presented in the same Fig. 1, in which a similar steplike behavior could be observed. For convenience, hereafter the pressure coefficient (namely, $\bar{C}_p$, the pressure normalized with the dynamic pressure at the outer flow and divided by a reference value) instead of the pressure itself is plotted, and our method is illustrated using the pressure at the surface of the airfoil, where no true shock wave is possible because the velocity is zero. The steep jumps in the pressure profiles encountered herein are of course due to nearby shock waves. In fact, in the case being treated, both the position of the shock wave structure and the associated pressure jump are poorly defined, as compared with the true shock waves that are encountered inside the flowfield, which would be more easily treated.

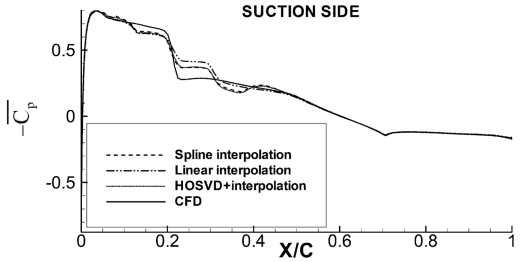

Fig. 1 Comparison of the CFD pressure coefficient and various approximations at test point P1− ($\alpha = +2.25$, $M = 0.800$, and $\delta = -2.50$).

Treatment of Shock Waves

The proposed method of dealing with shock waves is organized into three consecutive steps: 1) identifying the shock wave structures and disassembling each structure into a steep jump and a smooth profile, 2) applying the HOSVD to the two parts of the structure, and c) interpolating and assembling the separated parts so as to reconstruct the complete pressure profile. A description of the method is as follows (see Fig. 2):

Step 1: Identifying the shock wave structure and disassembling

1) Airfoil surface pressure distributions are plotted for the various snapshots resulting from CFD computations.

2) Search for that point (i.e., point Q_3 in Fig. 2) exhibiting the largest pressure steepness. This point locates the position of the shock wave (if any); namely, if this largest pressure steepness is smaller than a certain threshold value, P_{xm}, it is decided that no shock wave structure is present. Selection of P_{xm} requires some calibration.

3) Assume that the shock wave region extends to two grid points upstream (Q_1, Q_2) and three grid points downstream (Q_4, Q_5, Q_6) of the central point Q_3 already located; see Fig. 2.

4) Now, in the interval $Q_1, \ldots, Q_6$, the pressure distribution $P = P(x)$ is approximated as

$$P \cong P_{\text{jump}} + P_{\text{smooth}} \tag{7}$$

where P_{jump} accounts for the internal structure of the shock wave and is defined to exhibit a linear behavior in the interval $Q_1, \ldots, Q_6$ affected by the shock wave (Fig. 2), whereas P_{smooth} is defined to be constant in this interval (Fig. 2). Note that this is

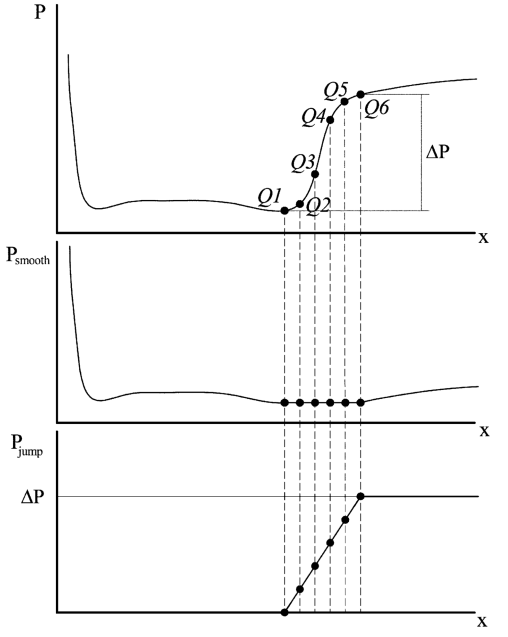

Fig. 2 Illustration of the methodology used to treat shock waves in the HOSVD approach.

a fairly primitive way of defining the shock wave structure, which can be greatly improved in various obvious ways, but is maintained in this paper to illustrate that the key point is to remove the pressure jump before applying HOSVD; the way in which this jump is removed leads to a second-order improvement.

5) Note that the linear structure of P_{jump} only depends on the position of the central point, Q_3, and the pressure jump (between Q_1 and Q_6), ΔP, which are both measured and stored, as is the pressure profile associated with P_{smooth}.

At this stage, anticipating that the test problem is characterized by three parameters (the Mach number M, the angle of attack α, and the flap deflection angle δ), the following quantities are to be stored: $Q_3(M,\alpha,\delta)$, $\Delta P(M,\alpha,\delta)$, and $P_{\text{smooth}}(x,M,\alpha,\delta)$. After discretization, the scalars Q_3 and ΔP are defined by two third-order tensors, and P_{smooth} requires consideration of a fourth-order tensor. Note that Q_3 and ΔP are only defined at those parameter values for which a shock wave structure exists; $\Delta P = 0$ is set at the remaining parameter values, but Q_3 is let undefined.

Step 2: Application of the HOSVD

1) Apply the aforementioned HOSVD method to the tensors associated with the quantities ΔP and P_{smooth} and truncate the associated decompositions to store these quantities with a previously specified error.

Step 3: Interpolation and assembling of the separated elements

1) Once the HOSVD reconstruction is available for the variables ΔP and P_{smooth}, approximations are available for these two quantities at the nodes of the mesh in the parameter space where the snapshots have been calculated. ΔP and P_{smooth} at other parameter values are obtained by cubic spline interpolation. In fact, it is the HOSVD modes associated with ΔP and P_{smooth} and not the whole reconstructed tensors that are interpolated, which only requires 1-D interpolation. For instance, if the reconstructed pressure field (6) is given by the extension of Eq. (2) to fourth-order tensors, namely,

$$P(M_i,\alpha_j,\delta_k,x_l) \equiv P_{ijkl} = \sum_{i_1=1}^{r_1}\sum_{j_1=1}^{r_2}\sum_{k_1=1}^{r_3}\sum_{l_1=1}^{r_4}\sigma_{i_1 j_1 k_1 l_1} u_{i i_1} v_{j j_1} w_{k k_1} x_{l l_1} \tag{8}$$

then interpolation is made in each of the modes u_{ii_1}, v_{jj_1}, and w_{kk_1} associated with each of the three parameters and not with the whole tensor P_{ijkl}. The interpolation of shock wave position Q_3 is performed in a different way. The reason is that this quantity is only defined at those values of the parameters for which the shock wave structure exists; thus, HOSVD methodology is not possible. Because a 3-D parameter space is considered, each newly reconstructed point is surrounded by $2^3 = 8$ snapshots. It is assumed that a shock wave is present at the reconstructed point if at least four neighboring snapshots show a shock wave. If this is the case, Q_3 is computed using a linear 3-D least-squares approximation from the neighboring points that exhibit the discontinuity.

2) The final assembling is made following the method described in step 1 in a backward fashion, namely, reconstructing the whole pressure profile using Eq. (7).

Practical examples of this methodology are presented next.

Test Problem

The freestream flow around the 2-D isolated airfoil shown in Fig. 3 at the fixed Reynolds number of 20×10^6 is considered. Three additional parameters, namely, the Mach number M, the angle of attack α, and the flap deflection angle δ, are varied in the ranges of 0.4–0.8, $-3-+3$ deg, and $-5-+5$ deg, respectively. A flap hinge (not shown in Fig. 3, but slightly appreciated in Fig. 8b) exists at the station located 0.6 chord lengths away from the airfoil leading edge. The range of parameters considered yields flow topologies that differ significantly from each other, as shown in the iso-Mach contours

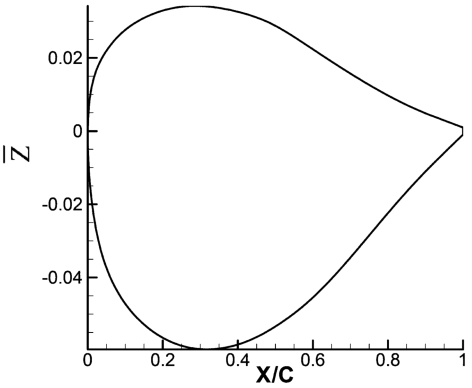

Fig. 3 Airfoil profile shape in the x–z plane used for method testing purposes. A flap hinge exists at the station $x = 0.6$ that is not shown in this figure.

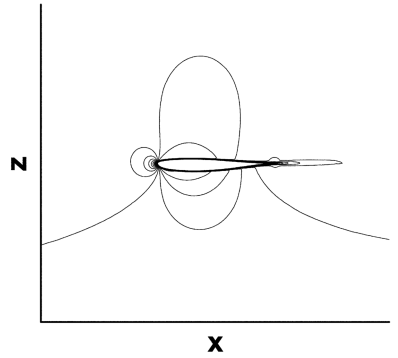

Fig. 4 Iso-Mach contours in the x–z plane corresponding to $\alpha = +0.00$, $M = 0.400$, and $\delta = +0.00$.

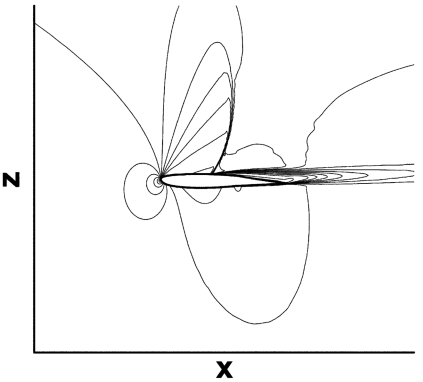

Fig. 5 As Fig. 4, for $\alpha = +3.00$, $M = 0.800$, and $\delta = +5.00$.

plotted in Figs. 4–7 for representative values of the parameters. In particular, the flow depicted in Fig. 4 ($M = 0.40$, $\alpha = 0$ deg, $\delta = 0$ deg) is attached and presents no shock wave. A suction side shock wave and a large separated flow region can be observed in Fig. 5 ($M = 0.80$, $\alpha = +3$ deg, $\delta = +5$ deg), whereas Fig. 6 ($M = 0.80$, $\alpha = +2$ deg, $\delta = -1$ deg) shows both pressure and suction side shock waves. Finally, a pressure side shock wave and a large separated flow region are present in Fig. 7 ($M = 0.80$, $\alpha = -3$ deg, $\delta = -5$ deg).

The CFD computations needed to generate the snapshots for the HOSVD analysis have been performed using the TAU code [17,18] with the version of the Edwards-corrected Spalart–Allmaras turbulence model [19]. The computational domain, which contains 55,578 elements, is shown in Figs. 8a (generic computational domain overview) and 8b (close-up view of the mesh in the vicinity of the airfoil). The outer boundary of the domain, accounting for the freestream flow, was located 50 chords away from the airfoil. For the

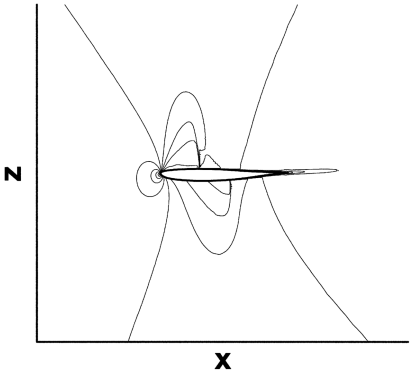

Fig. 6 As Fig. 4, for $\alpha = +2.00$, $M = 0.800$, and $\delta = -1.00$.

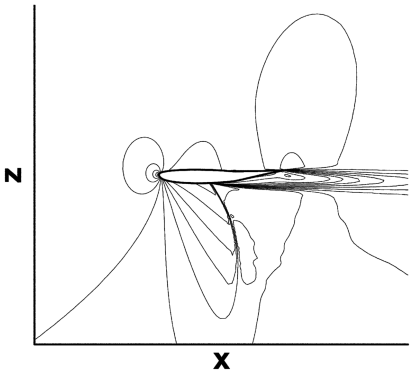

Fig. 7 As Fig. 4, for $\alpha = -3.00$, $M = 0.800$, and $\delta = -5.00$.

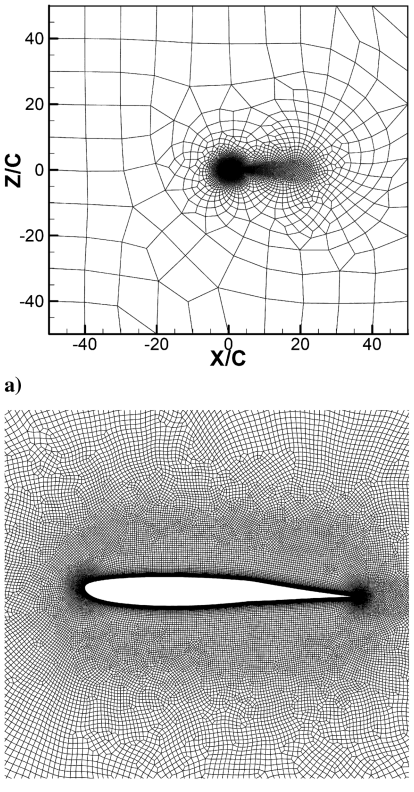

Fig. 8 Generic overview of the computational domain (a) and close-up view of the mesh in a vicinity of the airfoil in the x–z plane (b).

Table 1 Coordinates of the selected test points in the parametric space $\alpha - M - \delta$

Test point	Mach	α, deg	δ, deg
P1+	0.800	+2.25	+2.50
P1−	0.800	+2.25	−2.50
P3+	0.725	+2.25	+2.50
P3−	0.725	+2.25	−2.50
P5+	0.525	+2.25	+2.50
P5−	0.525	+2.25	−2.50
P2+	0.800	−2.25	+2.50
P2−	0.800	−2.25	−2.50
P4+	0.725	−2.25	+2.50
P4−	0.725	−2.25	−2.50
P6+	0.525	−2.25	+2.50
P6−	0.525	−2.25	−2.50
P11+	0.800	+1.25	+2.50
P11−	0.800	+1.25	−2.50
P13+	0.725	+1.25	+2.50
P13−	0.725	+1.25	−2.50
P15+	0.525	+1.25	+2.50
P15−	0.525	+1.25	−2.50
P12+	0.800	−1.25	+2.50
P12−	0.800	−1.25	−2.50
P14+	0.725	−1.25	+2.50
P14−	0.725	−1.25	−2.50
P16+	0.525	−1.25	+2.50
P16−	0.525	−1.25	−2.50

cases with a flap deflection different from zero, the total number of elements is kept and the mesh is deformed in the region near the wall. In all cases, 393 elements modeled the airfoil surface.

To assess the behavior of the method, the aerodynamic coefficients (namely, the lift, drag, momentum, and flap momentum) are reconstructed in a series of 24 test points, listed in Table 1, whose location in the parametric plane $\alpha - M$ is illustrated in Fig. 9, which applies to the two flap deflection angles that have defined in Table 1. Also, the method is evaluated for three different combinations of snapshots (none of which coincide with the test points, cf. Table 1), which correspond to the rectangular meshes of the parameter space:

Combination 1 ($9 \times 13 \times 9 = 1053$ snapshots) for the following parameter values:

1) $M = 0.40, 0.45, 0.50, 0.55, 0.60, 0.65, 0.70, 0.75$, and 0.80.
2) $\alpha = -3.00, -2.50, -2.00, -1.50, -1.00, -0.50, 0.00, 0.50, 1.00, 1.50, 2.00, 2.50$, and 3.00.

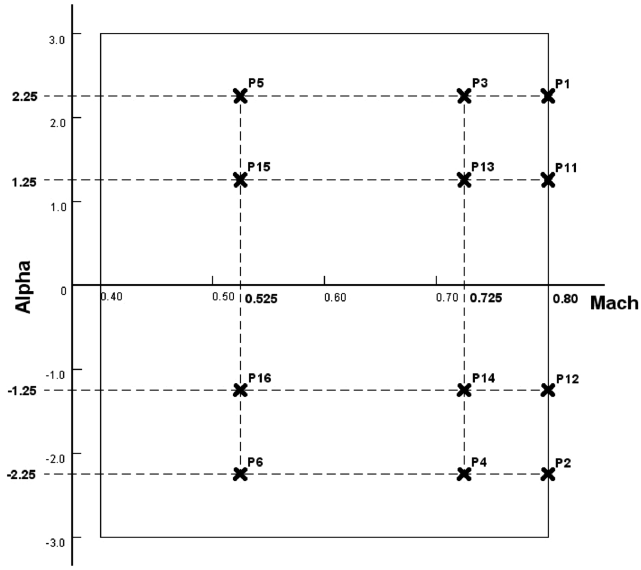

Fig. 9 Location of the selected test points in the parametric plane $\alpha - M$.

3) $\delta = -5.00, -3.00, -2.00, -1.00, 0.00, 1.00, 2.00, 3.00$, and 5.00.

Combination 2 ($6 \times 9 \times 7 = 378$ snapshots) for the following parameter values:

1) $M = 0.40, 0.55, 0.65, 0.70, 0.75$, and 0.80.
2) $\alpha = -3.00, -2.50, -1.50, -1.00, 0.00, 1.00, 1.50, 2.50$, and 3.00.
3) $\delta = -5.00, -3.00, -2.00, 0.00, 2.00, 3.00$, and 5.00.

Combination 3 ($4 \times 5 \times 5 = 100$ snapshots) for the following parameter values:

1) $M = 0.40, 0.55, 0.70$, and 0.80.
2) $\alpha = -3.00, -1.50, 0.00, 1.50$, and 3.00.
3) $\delta = -5.00, -3.00, 0.00, 3.00$, and 5.00.

Results

Two different approaches have been followed to apply HOSVD to the problem under consideration:

1) In approach 1, HOSVD plus interpolation, as described, is applied to the local pressure distribution $P(x)$ along the airfoil, using a threshold value that has been defined after some calibration to define shock waves $P_{xm} = 0.09$. Then, the lift, momentum, and flap momentum coefficients, C_L, C_M, and C_{FM}, and the pressure part of the drag coefficient, C_{PD}, are computed integrating the appropriate projection of the reconstructed $P(x)$ profile. C_M is measured with respect to a point located at a distance of 0.25 chords from the leading edge. C_{FM} is measured with respect to the flap hinge. The viscous part of the drag coefficient, or friction drag coefficient, C_{FD}, cannot be calculated from the pressure distribution and is obtained by applying HOSVD plus interpolation to the global C_{FD} coefficient obtained after the CFD results.
2) In approach 2, HOSVD is applied to the global aerodynamic coefficients, C_L, C_M, C_{FM}, and C_{PD}, thereby renouncing the gathering of local information on the pressure distribution along the airfoil.

The results obtained with both approaches are presented in Tables 2–5. They have been scaled with the minimum and maximum values of the CFD results as follows: $\bar{\Phi} = (\Phi - \Phi_{\min \mathrm{CFD}})/(\Phi_{\max CFD} - \Phi_{\min \mathrm{CFD}})$, where Φ stands for any of the aerodynamic coefficients; thus, absolute errors are, in fact, relative errors.

Results of Approach 1:

Regarding global aerodynamic coefficients, the average prediction errors associated with the 24 selected test points for the cases with 1053, 378, and 100 snapshots are as follows:

1) C_L: 1.1, 2.2, and 5.0%, respectively.
2) C_M: 2.9, 6.0, and 14.2%, respectively.
3) C_{FM}: 3.8, 8.0, and 20.6%, respectively.
4) C_D: 2.4, 5.8, and 11.4%, respectively.

Results of Approach 2:

Concerning global aerodynamics coefficients, the average prediction errors associated with the 24 selected test points for the cases with 1053, 378, and 100 snapshots are as follows:

1) C_L: 0.2, 0.3, and 1.0%, respectively.
2) C_M: 0.6, 0.7, and 2.4%, respectively.
3) C_{FM}: 0.8, 0.9, and 2.5%, respectively.
4) C_D: 0.7, 1.1, and 3.2%, respectively.

These results show that approach 2 with 378 snapshots presents the most favorable balance between accuracy and computational cost to determine global coefficients. Increasing the number of snapshots from 378 to 1053 increases the computational time by a factor of nearly 3 with a very small improvement in prediction accuracy. This is seemingly due to the fact that the combination of 378 snapshots provides a HOSVD error that is comparable to that of CFD (of the order of 1%, roughly). On the other hand, using 100 snapshots instead of 378 allows for saving computational time by a factor of nearly 4, but the average error is somewhat larger (in the range of 1–3%). Nevertheless, the case with 100 snapshots still yields reasonable accuracy at a low computational cost, which means that this case is attractive for quick predimensioning purposes in the early stages of a practical design problem. Approach 1 generates errors in the global aerodynamic coefficients that are larger than those in approach 2. In particular (see Figs. 11 and 12), the case with 100 snapshots does not provide the necessary accuracy for the local pressure distribution, and the average prediction errors using 378 snapshots are in the range of 2–8%. This was to be expected because gathering additional information on the behavior of the local pressure field does not come for free, but worsens the prediction accuracy of the global parameters. If both global and local precision are sought, it would be necessary to pay the price of computing 1053 snapshots. Figures 10–12 show the reconstructed local pressure distributions for the cases of 1053, 378,

Table 2 Reconstructed lift coefficient and comparison with the CFD results

C_L		HOSVD 1			HOSVD 2		
Test point	CFD	1053 snapshots	378 snapshots	100 snapshots	1053 snapshots	378 snapshots	100 snapshots
P1+	1.000	0.995	0.995	0.983	1.000	0.999	0.997
P1−	0.503	0.499	0.504	0.493	0.501	0.502	0.493
P3+	0.932	0.940	0.940	0.950	0.937	0.938	0.921
P3−	0.535	0.549	0.561	0.501	0.537	0.538	0.536
P5+	0.850	0.850	0.852	1.092	0.849	0.850	0.843
P5−	0.556	0.557	0.581	0.549	0.557	0.558	0.561
P2+	0.339	0.336	0.336	0.356	0.339	0.334	0.354
P2−	0.196	0.199	0.196	0.212	0.198	0.193	0.203
P4+	0.366	0.373	0.365	0.383	0.361	0.359	0.370
P4−	0.000	0.036	0.038	0.029	0.022	0.020	0.034
P6+	0.438	0.437	0.426	0.435	0.436	0.438	0.432
P6−	0.144	0.211	0.324	0.073	0.146	0.142	0.161
P11+	0.878	0.889	0.893	1.055	0.882	0.885	0.901
P11−	0.366	0.393	0.395	0.522	0.366	0.368	0.364
P13+	0.802	0.808	0.807	0.826	0.799	0.799	0.805
P13−	0.412	0.385	0.372	0.444	0.410	0.411	0.418
P15+	0.759	0.752	0.677	0.597	0.757	0.758	0.755
P15−	0.464	0.465	0.466	0.470	0.466	0.467	0.470
P12+	0.443	0.439	0.438	0.437	0.443	0.438	0.442
P12−	0.230	0.234	0.230	0.235	0.232	0.228	0.234
P14+	0.494	0.493	0.499	0.475	0.493	0.494	0.483
P14−	0.086	0.097	0.099	0.121	0.086	0.089	0.130
P16+	0.530	0.529	0.533	0.526	0.528	0.529	0.522
P16−	0.236	0.229	0.262	0.320	0.237	0.237	0.251

Table 3 Reconstructed moment coefficient and comparison with the CFD results

C_M		HOSVD 1			HOSVD 2		
Test point	CFD	1053 snapshots	378 snapshots	100 snapshots	1053 snapshots	378 snapshots	100 snapshots
P1+	0.000	0.020	0.020	0.011	−0.001	0.007	0.014
P1−	0.936	0.943	0.007	0.924	0.941	0.948	0.967
P3+	0.290	0.305	0.014	0.305	0.295	0.293	0.220
P3−	0.730	0.650	0.080	0.606	0.723	0.722	0.761
P5+	0.198	0.197	0.001	0.197	0.195	0.194	0.184
P5−	0.611	0.609	0.001	0.554	0.610	0.611	0.611
P2+	0.414	0.427	0.012	0.422	0.410	0.410	0.359
P2−	0.868	0.860	0.007	0.858	0.863	0.869	0.863
P4+	0.164	0.136	0.028	0.139	0.161	0.161	0.202
P4−	0.757	0.703	0.054	0.702	0.719	0.719	0.678
P6+	0.193	0.191	0.002	0.225	0.192	0.192	0.195
P6−	0.603	0.425	0.178	0.097	0.602	0.608	0.612
P11+	0.162	0.127	0.035	0.104	0.152	0.148	0.091
P11−	1.000	0.919	0.081	0.932	1.000	0.993	1.007
P13+	0.226	0.236	0.010	0.239	0.238	0.238	0.188
P13−	0.726	0.802	0.076	0.839	0.715	0.716	0.764
P15+	0.193	0.206	0.013	0.393	0.192	0.191	0.183
P15−	0.611	0.612	0.000	0.608	0.610	0.612	0.620
P12+	0.298	0.321	0.023	0.311	0.297	0.303	0.302
P12−	0.902	0.892	0.010	0.889	0.895	0.902	0.902
P14+	0.189	0.169	0.020	0.156	0.178	0.177	0.206
P14−	0.720	0.715	0.005	0.709	0.748	0.746	0.693
P16+	0.193	0.191	0.001	0.182	0.191	0.192	0.193
P16−	0.609	0.627	0.018	0.558	0.608	0.601	0.621

Table 4 Reconstructed flap momentum coefficient and comparison with the CFD results

C_{FM}		HOSVD 1			HOSVD 2		
Test point	CFD	1053 snapshots	378 snapshots	100 snapshots	1053 snapshots	378 snapshots	100 snapshots
P1+	0.000	0.027	0.027	−0.025	0.000	−0.003	0.009
P1−	0.565	0.568	0.003	0.558	0.576	0.579	0.618
P3+	0.022	0.030	0.008	0.035	0.033	0.033	−0.003
P3−	0.581	0.456	0.125	0.394	0.585	0.588	0.600
P5+	0.018	0.014	0.004	0.010	0.012	0.009	0.003
P5−	0.530	0.531	0.001	0.453	0.530	0.533	0.542
P2+	0.318	0.339	0.021	0.350	0.306	0.306	0.276
P2−	1.000	0.999	0.001	0.996	0.997	0.997	1.006
P4+	0.239	0.222	0.016	0.220	0.218	0.215	0.233
P4−	0.679	0.752	0.072	0.749	0.752	0.748	0.761
P6+	0.258	0.252	0.006	0.295	0.252	0.255	0.242
P6−	0.759	0.514	0.245	0.075	0.761	0.755	0.791
P11+	0.125	0.083	0.042	0.049	0.127	0.127	0.139
P11−	0.683	0.577	0.106	0.605	0.676	0.676	0.694
P13+	0.056	0.048	0.008	0.053	0.045	0.045	0.052
P13−	0.632	0.726	0.094	0.780	0.627	0.630	0.661
P15+	0.070	0.087	0.017	0.361	0.067	0.067	0.055
P15−	0.583	0.586	0.004	0.583	0.585	0.585	0.597
P12+	0.120	0.156	0.036	0.139	0.115	0.112	0.106
P12−	0.912	0.908	0.004	0.904	0.909	0.903	0.924
P14+	0.189	0.156	0.033	0.144	0.185	0.188	0.161
P14−	0.678	0.682	0.004	0.685	0.682	0.685	0.773
P16+	0.204	0.199	0.005	0.187	0.200	0.200	0.185
P16−	0.711	0.739	0.028	0.648	0.712	0.715	0.733

and 100 snapshots and a comparison with the CFD profiles for three different test cases, namely P1−, P4+, and P11+. These figures show that the case with 378 snapshots provides a sufficiently accurate prediction of the pressure field for a practical design situation, for instance, the computation of local loads on the airfoil. Note also that the proposed methodology offers a good description of the local pressure field in the vicinity of the flap hinge. When looking at the global results obtained by using approach 1 (see Tables 2–5), it is apparent that in test case P6− the results are far off the mark. The reason for this very poor behavior is that this test case corresponds to the situation in which the least-squares interpolation of the shock position inside the parametric space does not lead to a consistent solution. In particular, the CFD solution of this test point presents a weak shock wave whereas the criterion used states that no shock wave is present (see Fig. 13). As described earlier, this anomalous behavior might occur in the region of the parametric space where the shock wave is about to disappear. Nevertheless, these cases occur at lower Mach numbers (0.525 in our case) and they do not drive the airfoil design. Furthermore, as seen in Tables 2–5, the results obtained for this case when using approach 2 are accurate again.

Finally, it is to be noted that the computational cost of reconstruction is negligible for both approaches 1 and 2. In particular, using approach 2, the aerodynamic coefficients of each test point are obtained in less than one-tenth of a second when using a desktop personal computer with a 3.4 GHz CPU.

Table 5 Reconstructed drag coefficient and comparison with the CFD results

C_D		HOSVD 1			HOSVD 2		
Test point	CFD	1053 snapshots	378 snapshots	100 snapshots	1053 snapshots	378 snapshots	100 snapshots
P1+	0.641	0.640	0.001	0.598	0.642	0.622	0.601
P1−	0.102	0.111	0.009	0.088	0.101	0.090	0.163
P3+	0.144	0.128	0.016	0.126	0.139	0.137	0.200
P3−	0.012	−0.026	0.038	−0.057	0.002	0.002	0.041
P5+	0.011	0.005	0.007	−0.010	0.011	0.006	0.024
P5−	0.004	0.016	0.012	0.054	0.002	0.002	0.006
P2+	0.518	0.511	0.007	0.488	0.519	0.506	0.498
P2−	1.000	0.986	0.014	0.977	0.994	0.983	0.981
P4+	0.024	−0.008	0.033	−0.013	0.032	0.019	0.124
P4−	0.540	0.463	0.077	0.454	0.494	0.481	0.401
P6+	0.003	0.006	0.003	0.035	0.002	0.002	0.013
P6−	0.023	−0.187	0.210	−0.582	0.026	0.028	0.028
P11+	0.211	0.195	0.016	0.179	0.217	0.210	0.264
P11−	0.270	0.270	0.000	0.255	0.262	0.251	0.240
P13+	0.025	0.004	0.020	0.004	0.009	0.009	0.052
P13−	0.013	0.046	0.033	0.040	−0.006	−0.006	0.049
P15+	0.005	−0.007	0.011	−0.125	0.004	0.006	0.011
P15−	0.004	0.009	0.006	0.003	0.004	0.004	0.011
P12+	0.217	0.209	0.008	0.206	0.219	0.210	0.221
P12−	0.749	0.735	0.013	0.725	0.740	0.730	0.740
P14+	0.008	−0.006	0.014	−0.018	−0.002	−0.011	0.047
P14−	0.196	0.189	0.007	0.176	0.227	0.217	0.159
P16+	0.000	0.002	0.002	−0.005	0.000	0.000	0.006
P16−	0.014	0.024	0.010	−0.036	0.015	0.009	0.039

Conclusions

A HOSVD-based method has been presented to generate aerodynamic databases using a limited number of CFD computations. In particular, the work has focused on the treatment of the shock waves, which is necessary because these localized structures are not (in principle) well suited for analysis with SVD-like methods. It has been found that our approach is robust and yields results that are dramatically better than those obtained using standard HOSVD, as can be seen by comparing Figs. 1 and 10. In addition, our method could be used in practical aerodynamics design applications. In particular, the method could be applied to databases described by parametric spaces that encompass flowfields of a different nature. This is important because one of the main worries that the engineer may have when looking forward to industrial applications is that the tool that he is going to use could need to be assessed every single time, over and over again. In our test problem, the main worry was that the method would work only on topologically similar flowfields. If this were the case, the engineer would have need to classify by himself, as a kind of preprocessing work, the different CFD snapshots into families, namely, snapshots with a shock wave on the pressure side, snapshots with a shock wave on the suction side, snapshots with two shock waves, and so on. However, it has been found that the method is able to deal with the whole parametric space all at once, without significant accuracy degradation. In particular, with only 378 snapshots, the method allows for the reconstruction of a whole database characterized by three different parameters (Mach number, angle of attack, and flap deflection) with an error in the aerodynamic coefficients that is always less than 1%. Also, it has been shown that it is possible to reconstruct the local pressure coefficient with a similar level of precision.

The main ingredient in our method, namely, the removal of the internal shock wave structure before applying HOSVD, was made in a fairly rough way. This was done on purpose, to illustrate that the

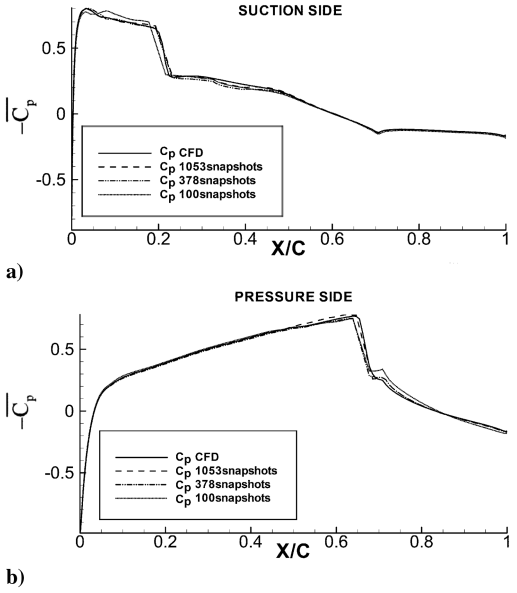

Fig. 10 Comparison of the CFD and reconstructed pressure coefficient in the case of test point P1−.

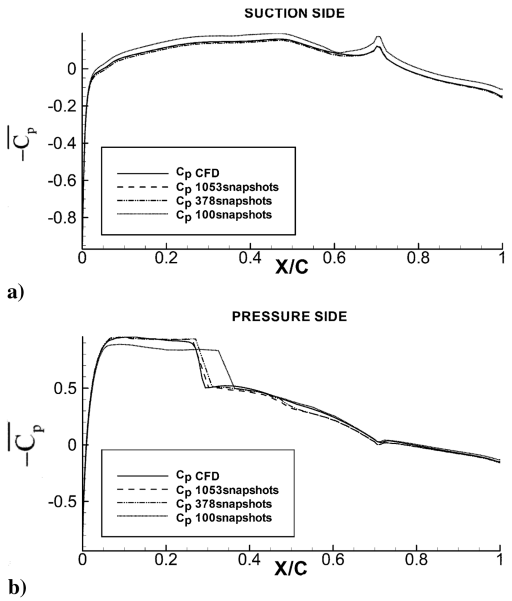

Fig. 11 As Fig. 10, for the test point P4+.

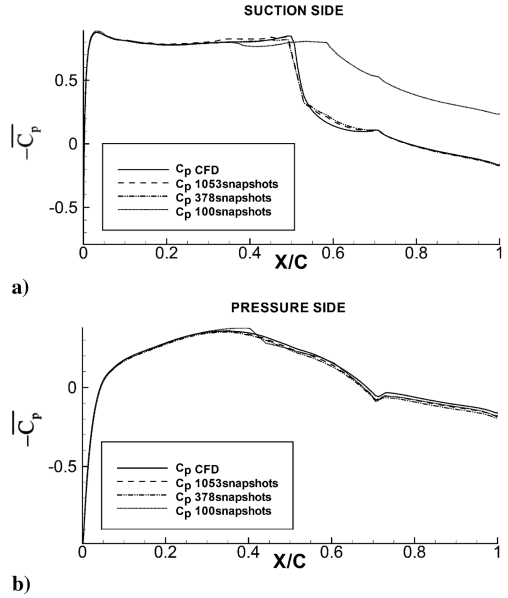

Fig. 12 As Fig. 10, for the test point P11+.

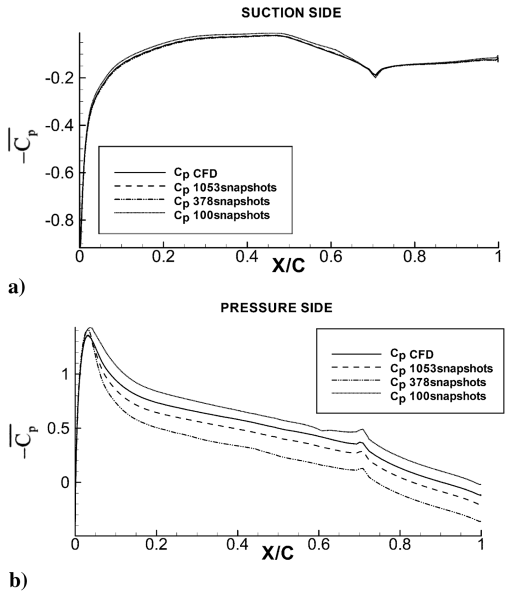

Fig. 13 As Fig. 10, for the test point P6−.

main benefit comes from removing the shock wave structure, and not from the way this is done. Several possible removing strategies are being evaluated and will be presented elsewhere.

In addition, it has been found that increasing the amount of available information using 1053 snapshots did not improve accuracy significantly, whereas getting down to 100 snapshots degraded the quality of the results. That is, for a prescribed level of error, there is an optimum amount of information (number of snapshots) that, once reached, does not need improvement. In this frame, the desirable goal, from the practical engineering point of view, would be to be able to estimate this optimum amount of information beforehand, so that the aerodynamics design cycle would be further shortened and its cost lowered even more. Note that the optimal number of snapshots depends on the required error of the process and also on how they are distributed in the parameter space. In this paper, snapshots have been considered to be in a rectangular, essentially equispaced grid in the parameter space, but this needs not be optimal. A search for optimal (in terms of computational cost) distributions of snapshots is the main object of our ongoing work.

Finally, concerning practical industrial application, it has been concluded that approaches 1 and 2 should be used in parallel at different stages of the design and/or database generation process. In particular, with a relatively small number of snapshots (100), approach 2 delivers global coefficients with an accuracy that is sufficient for the early stages of the design process. If more accurate information on the global coefficients or local pressure information is needed later on, approaches 1 and 2 with 378 snapshots provide the required answer. In other words, it is more practical (and less expensive) to work with the two different approaches and apply them as required by the industrial environment rather than trying to combine them both in a single tool. Specifically, this is because of the fact that the computational cost of the HOSVD is so small that the cost of the method is fully associated to the cost of computing the snapshots.

Acknowledgments

This research project has been funded by Airbus (contract A8208636G). The authors are, in addition, indebted to Carlos Artiles of Airbus for his continuous guidance in the precise identification of the relevant requirements of the method in terms of daily engineering needs and to Markus Wildham of the DLR, German Aerospace Center for his assistance with the TAU computations. One of the authors, J. M. Vega, has also been partially supported by project TRA2007-65699/TAIR of the Spanish Ministry of Education and Science.

References

[1] Bui-Thanh, T., "Proper Orthogonal Decomposition Extensions and their Applications in Steady Aerodynamics," Master's Thesis, Singapore–Massachusetts Institute of Technology Alliance, 2003.

[2] Bui-Thanh, T., Damodaran, M., and Willcox, K., "Aerodynamic Data Reconstruction and Inverse Design Using Proper Orthogonal Decomposition", *AIAA Journal*, Vol. 42, No. 8, 2004, 1505–1516. doi:10.2514/1.2159

[3] Tang, D., Kholodar, D., Juang, J-N., and Dowell, E. H., "System Identification and Proper Orthogonal Decomposition Method Applied to Unsteady Aerodynamics," *AIAA Journal*, Vol. 39, No. 8, 2001, 1569–1576.

[4] Kim, Y., Rockwell, D., and Liakopoulos, A., "Vortex Buffeting of Aircraft Tail: Interpretation via Proper Orthogonal Decomposition," *AIAA Journal*, Vol. 43, No. 3, 2005, 550–559. doi:10.2514/1.9989

[5] LeGresle, P., and Alonso, J., "Investigation of Non-Linear Projection for POD Based Reduced Order Models for Aerodynamics," AIAA Paper 2001-0926, 2001.

[6] Dowell, E., Hall, K., Thomas, J., Florea, R., Epureanu, B., and Hegg, J., "Reduced Order Models in Unsteady Aerodynamics," AIAA Paper 99-1261, 1999.

[7] Hall, K. C., Thomas, J. P., and Dowell, E. H., "Proper Orthogonal Decomposition Technique for Transonic Unsteady Aerodynamic Flows," *AIAA Journal*, Vol. 38, No. 10, 2000, 1853–1862.

[8] Romanousk, M., "Reduced Order Unsteady Aerodynamics and Aerolastic Models Using Karhunen-Loeve Eigenmodes," AIAA Paper 96-3981, 1996.

[9] Willcox, K, and Peraire, J., "Balanced Model Reduction via the Proper Orthogonal Decomposition," *AIAA Journal*, Vol. 40, No. 11, 2002, 2323–2330.

[10] Lucia, D. J., Beran, P. S., and Silva, W. A., "Aeroelastic System Developments Using Proper Orthogonal Decomposition and Volterra Theory," *Journal of Aircraft*, Vol. 42, No. 2, 2005, 509–518. doi:10.2514/1.2176

[11] Munteanu, S., Ragadas, J., Nam, C., and Chattopadhyay, A., "Reduced Order Model Approach for Aeroelastic Analysis Involving Aerodynamic and Structural Nonlinearities," *AIAA Journal*, Vol. 43, No. 3, 2005, 560–571. doi:10.2514/1.10971

[12] Thomas, J. P., Dowell, E. H., and Hall, K. C., "Three-Dimensional Transonic Aeroelasticity Using Proper Orthogonal Decomposition-Based Reduced-Order Models," *Journal of Aircraft*, Vol. 40, No. 3, 2003, 544–551.

[13] Lucia, D., Beran, P., and Silva, W., "Reduced Order Modelling: New Approach for Computational Physics," *Progress in Aerospace Sciences*, Vol. 40, Nos. 1–2, 2004, 51–117.

doi:10.1016/j.paerosci.2003.12.001
[14] Golub, G. H., and Van Loan, G. T. *Matrix Computations*, John Hopkins Univ. Press, 1996.
[15] De Oathauwer, L., De Moor, B., and Vandewalle, J., "On the Best Rank-One and Rank-($R_1, R_2, \ldots, R_N$) Approximation of Higher Order Tensors," *SIAM Journal on Matrix Analysis and Applications*, Vol. 21, No. 4, 2000, 1324–1342.
doi:10.1137/S0895479898346995
[16] da Silva, V., and Lim, L.-H. Tensor Rank and the Ill-Posedness of the Best Low-Rank Approximation Problem, *SIAM Journal on Matrix Analysis and Applications* (submitted for publication).
[17] Schwamborn, D., Gerhold, T., and Heinrich, R., "The DLR TAU-Code: Recent Applications in Research and Industry." European Community on Computational Methods in Applied Sciences Paper 619, Sept. 2006.
[18] Brodersen, O., Eisfeld, B., Raddatz, J., and Frohnapfel P., "DLR Results from the Third AIAA CFD Drag Prediction Workshop," AIAA Paper 2007-259, Jan. 2007.
[19] Edwards, J. R. "Comparison of Eddy Viscosity Transport Turbulence Models for Three Dimensional, Shock Separated Flow Fields." *AIAA Journal*, Vol. 34, No. 4, 756–763.
doi:10.2514/3.13137